International Journal of Plasticity 170 (2023) 103777

Contents lists available at ScienceDirect

International Journal of Plasticity

journal homepage: www.elsevier.com/locate/ijplas

Wavy interface enables extra strengthening in an additively manufactured high-entropy alloy with Mortise-Tenon architecture

Yunjian Bai [a,b], Yadong Li [a,b], Yun-jiang Wang [a,c], Kun Zhang [a,b,*], Quanyu Jiang [a,b], Zishang Liu [a,b], Zheng Hu [d], Bingchen Wei [a,b,*]

[a] Key Laboratory of Microgravity (National Microgravity Laboratory), Chinese Academy of Sciences, Institute of Mechanics, Beijing 100190, China
[b] School of Engineering Science, University of Chinese Academy of Sciences, Beijing 100049, China
[c] State Key Laboratory of Nonlinear Mechanics, Chinese Academy of Sciences, Institute of Mechanics, Beijing 100190, China
[d] Science and Technology on Vehicle Transmission Laboratory, China North Vehicle Research Institute, Beijing 100072, China

ARTICLE INFO

Keywords:
High entropy alloy
Laminated structure design
Additive manufacturing
Interface strengthening
Local chemical variation

ABSTRACT

Laminated structures have the potential to enhance the performance of high-entropy alloys (HEAs) by providing intriguing interface strengthening. However, laminated HEA designs is uncommon due to the challenges posed by the relatively poor machinability of HEAs. In this study, we successfully fabricate a CoCrNi-$Fe_{50}Mn_{30}Co_{10}Cr_{10}$ laminated HEA using additive manufacturing technique, incorporating a unique Mortise-Tenon architecture within the alloy. The laminated HEA introduces a novel wavy-shaped interface alongside the conventional flat-shaped interfaces. Tensile tests reveal that the laminated HEA exhibits an exceptional combination of strength and ductility. The measured yield strength exceeds the predicted value based on the rule-of-mixture principle by approximately 36.5 %. This enhancement is attributed to the extra strengthening resulting from the local chemical variation near the heterogeneous interfaces. Interestingly, the wavy-shaped interface has a larger local-chemical-variation zone than the flat-shaped interface, which can trigger more strong interface-dislocation interactions and therefore remarkable strengthening. The Mortise-Tenon architecture not only provides extra interface strengthening, surpassing the yield strength of the two monolithic HEAs, but also preserves the excellent work hardening ability in the early stage of deformation, enabling reasonable ductility. Remarkably, the interface strengthening is comparable in magnitude to dislocation strengthening, contributing to approximately 23 % of the overall yield strength. These findings highlight the potential of laminated HEA designs and the associated interface strengthening as promising strategies for enhancing mechanical performance.

1. Introduction

Over the past decade, high-entropy alloys (HEAs) have attracted profuse attention due to their unique design concepts, novel physical/chemical attributes, intriguing deformation mechanisms, and exceptional mechanical performance. The Cantor alloy, often regarded as the pioneer of the HEA community, is a prime example of the exceptional work hardening ability exhibited by HEAs,

* Corresponding authors at: Key Laboratory of Microgravity (National Microgravity Laboratory), Chinese Academy of Sciences, Institute of Mechanics, Beijing 100190, China.
E-mail addresses: zhangkun@imech.ac.cn (K. Zhang), weibc@imech.ac.cn (B. Wei).

https://doi.org/10.1016/j.ijplas.2023.103777
Received 25 July 2023; Received in revised form 9 October 2023;
Available online 10 October 2023

resulting in a favorable combination of strength and ductility (Cantor, 2021). More excitingly, the derivatives of the Cantor alloy exhibit more graceful mechanical properties, such as exceptionally high fracture toughness at cryogenic temperature (D. Liu et al., 2022), elegant transformation-induced plasticity (Li et al., 2016) and outstanding antiballistic capability (Tang and Li, 2022). Due to their excellent mechanical properties, HEAs are deemed as a new generation of excellent structural materials (Miracle and Senkov, 2017; Yeh et al., 2004).

Nevertheless, as the service environment/conditions (e.g., the extreme temperature, ultrahigh stress/strain, and ultrahigh strain rate) become increasingly challenging, higher demands are being placed on the performance of HEAs. Further improving the mechanical properties of HEAs and breaking through the inherent strength-ductility trade-off dilemma remain the research focus on HEAs. In recent years, thanks to the designs of heterogeneous structures (Sathiyamoorthi and Kim, 2022; Zhu and Wu, 2023), one can succeed in preparing HEAs with desired mechanical properties. Common heterogeneous HEA designs include dual- or multi-phase structures (He et al., 2021; Li et al., 2016; Ren et al., 2022; Wu et al., 2022), precipitate-matrix structures (L. Liu et al., 2022; Yang et al., 2018; 2021), gradient structures (Hasan et al., 2019a, 2019b; Pan et al., 2021; Qin et al., 2022; Zhang et al., 2023), and bimodal grained structures (Bai et al., 2023; 2021; Su et al., 2019; Wu et al., 2019; 2015), etc., which have shown great benefits in enhancement of mechanical properties. Ren et al. (2022) tailored nano-lamellae dual phase within $AlCoCrFeNi_{2.1}$ HEA using laser powder bed fusion, directly giving this alloy a high yield strength of 1.3 GPa and a considerable plasticity of 14 % without any thermal-mechanical post-treatment. Yang et al. (2018) designed $(FeCoNi)_{86}Al_7Ti_7$ HEA with ordered $L1_2$ nanoprecipitates embedded in disordered FCC matrix, enabling this alloy with a superior strength of 1.5 GPa and high ductility of 50 %. (Pan et al., 2021) introduced gradient nanoscale dislocation cells in $Al_{0.1}CoCrFeNi$ HEA, resulting in an almost twofold increase in the yield strength without significant loss of ductility, compared with its homogenized counterpart. These impressive achievements demonstrate that hetero-structure designs are a panacea for raising the upper bound of the mechanical properties of HEAs.

In addition to the above heterogeneous structures, laminated structure design with extensive heterogeneous interfaces is another extremely promising strengthening strategy (Chen et al., 2020; Huang et al., 2018; S. Liu et al., 2022; Ma et al., 2016; 2015; Wang et al., 2018, 2019; Wu et al., 2021). Note that the interface here refers exclusively to the component interface, not including grain or phase boundaries in the broad sense of "interface". The sides of the component interface will present severe heterogeneity such as grain size, texture, phase, strength, and chemical attribute (Ma et al., 2016). Consequently, this leads to strong interface strengthening, which has been evidenced in conventional metallic materials. For example, (Wang et al., 2019) investigated the mechanical properties of a laminated Cu-30 Zn composed of coarse-grained and fine-grained layers, and found that the heterogeneous interfaces enabled a superior strength-ductility synergy with extraordinary strengthening. (S. Liu et al., 2022) investigated the mechanical properties of an Mg-1Gd/Mn-13Gd laminate with heterogeneous grain size and texture, and found that this sample not only showed an excellent strength-ductility synergy but exhibited an improved ductility superior to the monolithic alloys. For the hidden mechanisms behind the interface strengthening, (Ma et al., 2016) suggested that it is due to the accumulation of profuse geometrically necessary dislocations (GNDs) because of the strong heterogeneity on both sides of the interface, resulting in considerable back-stress strengthening. Further, (Huang et al., 2018) confirmed that there existed an interface-affected-zone (IAZ) in heterogeneous laminates, effectively strengthening the target materials. Zhao et al. (2021) developed a dislocation density-based constitutive model and found that a smaller interface spacing implies a higher volume fraction in the IAZ.

Unfortunately, despite the promising of the interface strengthening, the laminated structure designs are uncommon in HEAs. A possible key reason is that the conventional methods (e.g., friction stir processing (Wang et al., 2019), accumulate roll bonding (Chen et al., 2020; Ma et al., 2016), and accumulate extrusion bonding (S. Liu et al., 2022)) used to fabricate laminated structures have high machining requirements. However, HEAs are usually not a single solid-solution because of their multicomponent features, and thus, a lot of HEAs have a relatively insufficient machining capability. On the other hand, the conventional methods for laminated structures often have a lengthy craft chain. For example, customizing an ultrafine interface spacing in a Cu-bronze laminate requires a large number of accumulate roll bonding cycles (Huang et al., 2018). One question naturally emerges whether there is an efficient and flexible path for producing laminated HEAs with excellent mechanical properties.

Additive manufacturing (AM) brings light to the solution to the above dilemma. AM fabricates the products by rapidly layer-by-layer printing and produce strong bonding between adjacent layers (DebRoy et al., 2018). Therefore, laminated HEA structures could be easily obtained by alternating deposition of two HEAs. More importantly, AM is a bottom-up approach to produce materials, which means that one can directly tailor a satisfactory layer size by setting suitable parameters in advance, not requiring any possible post-treatment. Up to now, only a few brief studies on laminated HEA designs via AM are available. Cai et al. (2021) fabricated a FeCoCrNi-FeCoCrNiAl laminated HEA by laser melting deposition. It is observed that the yield strength of the laminated HEA was larger than that of the pure FeCoCrNi HEA. (Guan et al., 2020) investigated the CrMnFeCoNi-$AlCoCrFeNiTi_{0.5}$ laminated HEA using laser-engineered net shaping. It is found that this laminated HEA showed strength-plasticity synergy. Unfortunately, the available research on laminated HEAs has been lacking in terms of providing comprehensive information on the microstructural characteristics, especially regarding the interfaces, both before and after deformation. Hence, although the huge potential shown by laminated HEA designs, the strengthening mechanisms and the role of the heterogeneous interface remains unclear, which severely limits the understanding of the laminated HEA designs and slows down their utilities as structural materials.

In this work, to gain an in-depth knowledge of the mechanical properties and deformation/strengthening mechanisms of the laminated HEAs with extensive heterogeneous interfaces, a CoCrNi-$Fe_{50}Mn_{30}Co_{10}Cr_{10}$ laminated HEA was fabricated using AM technique. We conducted a detailed investigation of the microstructural evolution within the two components, including grain size, texture, dislocation density and chemistry, both before and after the introduction of the laminated structure. We also examined the microstructures of the laminated HEA before and after deformation by extensive electron microscopic techniques. The tensile properties of the laminated HEA and the two monolithic HEAs were compared. All the strengthening mechanisms to the strength

contribution in the laminated HEA were elucidated and the corresponding values were calculated. Worth mentioning, the role of the interfaces between the CoCrNi layers and the $Fe_{50}Mn_{30}Co_{10}Cr_{10}$ layers for the resistance to dislocation motion and the resultant interface strengthening was highlighted, which would provide an insightful view for understanding of laminated HEA structures.

2. Experimental procedure

2.1. Laminated HEA preparation

The pre-alloyed powders (purity $\geq$ 99.9 %) of the CoCrNi and $Fe_{50}Mn_{30}Co_{10}Cr_{10}$ HEAs were prepared by vacuum induction melting gas atomization. The powder size was controlled between 45 μm to 105 μm. To obtain a CoCrNi-$Fe_{50}Mn_{30}Co_{10}Cr_{10}$ laminated HEA, the two powders were alternatingly deposited using direct energy deposition under the high purity argon protective atmosphere. The laser parameters of the two HEAs are listed in Table 1. The scanning path is a "zigzag" shape. During printing, the scanning direction is rotated 90° between two adjacent layers to reduce residual stress. The dimensions of the final as-deposited laminated HEA are 30 × 30 × 30 mm^3. For comparison, the monolithic CoCrNi and $Fe_{50}Mn_{30}Co_{10}Cr_{10}$ HEA were also fabricated based on identical laser parameters and dimensions.

2.2. Mechanical testing

Dog-bone-shaped specimens were cut out on the as-deposited samples using electrical discharge machine wire cutting. The gage dimension was 10 × 2.5 × 1 mm^3. Prior to tensile tests, the dog-bone-shaped specimens were carefully ground and polished to remove the surface defects. Quasi-static uniaxial tensile tests were performed on an MTS Landmark electro-hydraulic servo mechanics test system at a steady strain rate of 5×10^{-4} s^{-1} at room temperature. An extensometer with a displacement resolution of 0.1 μm was utilized to measure the elongation. To ensure the reliability of the results, each sample underwent testing at least three times.

2.3. Microstructural characterization

To identify the phase composition of the two monolithic HEAs and the laminated HEA, an X-ray diffraction (XRD) pattern with Cu-Kα radiation (wavelength of 0.15406 nm, Smartlab 9 kW) was carried out with a scanning angle from 30° to 100° (2θ), and the step size is 0.05°($\Delta 2\theta$).

To clearly demonstrate the microstructural evolution before and after introducing the laminated structure, a scanning electron microscope (SEM JSM-7100F) equipped with electron backscatter diffraction (EBSD) was used to characterize the laminated HEA and the two monolithic HEAs. Electron channeling contrast imaging (ECCI) pattern was used to observe the morphology, where the CoCrNi layers and the $Fe_{50}Mn_{30}Co_{10}Cr_{10}$ layers in the laminated HEA were determined using the energy-dispersive spectroscope (EDS). EBSD observation was also used to analyze the role of the interfaces during deformation. The working distance and accelerating voltage for the SEM/ECCI/EBSD are 15 mm and 20 kV, respectively.

The as-printed laminated HEA was further characterized by the field emission transmission electron microscope (TEM JEOL JEM-2100F) operating at 200 kV. High-resolution TEM (HRTEM) was used to characterize the atomic scale structures and crystalline defects inside the samples. To investigate the effect of the interfaces on the plastic deformation, TEM observations were also carried out on the deformed laminated HEA.

All the samples for the XRD, EBSD, ECCI, and TEM measurements have been first ground using carbide paper from 400 to 3000 granulation. The samples for EBSD and ECCI observations were prepared by further vibration polishing to obtain good surface quality. The as-built samples for TEM observation were first carefully ground into foils with a thickness of ~70 μm. After ultrasonic cleaning under alcohol-soaked environment, the foils were finally ion-beam thinning (FEI-Scios2) to a suitable thickness. The TEM foils for the deformed sample were precisely prepared by focused ion beam technique.

3. Results

3.1. XRD pattern

Fig. 1(a) displays the XRD patterns. The CoCrNi HEA features a pure FCC solid-solution while the $Fe_{50}Mn_{30}Co_{10}Cr_{10}$ HEA exhibits FCC and HCP dual-phase structure. These findings align with earlier researches (Li et al., 2017; Niu et al., 2021; Weng et al., 2020). The

Table 1
Printing parameters of the two HEA powders.

Parameters	CoCrNi	$Fe_{50}Mn_{30}Co_{10}Cr_{10}$
Laser power	400 W	400 W
Scanning speed	10 m/s	10 m/s
Hatch spacing	0.5 mm	0.5 mm
Powder feed rate	2.3 g/min	1.7 g/min
Laser dimeter	1 mm	1 mm
Layer thickness	0.1 mm	0.1 mm

XRD analysis for the laminated HEA reveals the detection of both the FCC and HCP phases, which is expected given the composite nature of the two HEAs. However, the HCP phase seems in small amounts, resulting in relatively weak diffraction peaks. Fig. 1(b) shows that the enlarged view of the diffraction peak corresponding to the (200) crystal plane. The diffraction peak of the laminated HEA has a significant rightward deviation and a larger full width at half maximum (FWHM) compared with those of the individual HEAs. This suggests that the laminated structure leads to more severe lattice distortion, implying that there are more crystalline defects, such as dislocations generated in the laminated HEA. In addition, a larger FWHM means a smaller grain size.

3.2. Surface morphology and microstructural characteristics

The SEM image displays that the laminated HEA has alternating CoCrNi/$Fe_{50}Mn_{30}Co_{10}Cr_{10}$ structures, see Fig. 2(a). Through EDS mappings, the two HEA layers and the melt pool can be easily positioned. Interestingly, when the CoCrNi layer transitions to the $Fe_{50}Mn_{30}Co_{10}Cr_{10}$ layer, the interface is flat marked by the blue dashed lines. Vice versa, there is no visible flat interface; rather, it is a series of melt pool boundaries forming a wavy interface marked by the white dashed lines. Therefore, two types of the interface are formed: one is the flat-shaped interface due to the direct deposition of the CoCrNi HEA on the $Fe_{50}Mn_{30}Co_{10}Cr_{10}$ HEA; the other is the wavy-shaped interface, which may be attributed to the partial remelting of the underneath CoCrNi HEA during the $Fe_{50}Mn_{30}Co_{10}Cr_{10}$ HEA deposition. This is very different from those findings with only flat-shaped interface in AMed laminated HEAs (Guan et al., 2020; Yang et al., 2022). The maximum layer thickness of the $Fe_{50}Mn_{30}Co_{10}Cr_{10}$ HEA is 155±9 μm, while the CoCrNi HEA is 108±12 μm. Additionally, the EDS mappings portrayed a Mortise-Tenon (M-T) architecture, where the CoCrNi layer is Mortise-shaped, and the $Fe_{50}Mn_{30}Co_{10}Cr_{10}$ layer is Tenon-shaped.

Fig. 2(b) shows the ECCI images of the laminated HEA. Visibly, the laminated HEA is mainly composited by columnar grains. A large view of the CoCrNi/ $Fe_{50}Mn_{30}Co_{10}Cr_{10}$ lamellae is illustrated in Fig. 2(c). The $Fe_{50}Mn_{30}Co_{10}Cr_{10}$ layer contains numerous needle-like HCP phase embedded in the FCC matrix. Fig. 2(d) confirms this observation. The needle-like HCP phase is relatively fine, of which width is the magnitude of the submicron level. In addition, the HCP phase is decorated with some cellular structures. Whereas the CoCrNi HEA is the pure FCC solid-solution without any second phase or particle. Fig. 2 indicate that the laminated HEA retains the original HEA categories while introducing a unique M-T skeleton.

To obtain quantitative information on the microstructural evolution before and after the introduction of the laminated structure, EBSD results are presented in Fig. 3. Inverse pole figure (IPF) maps reflect the information about the grain size, morphology, and orientation. In the $Fe_{50}Mn_{30}Co_{10}Cr_{10}$ HEA, both columnar and equiaxed grains are observed, and their orientation is random. The average grain size is 36 ± 40 μm. The CoCrNi HEA is mainly composed of columnar grains that are also randomly oriented without any texture, and the average grain size is 55 ± 65 μm. In the laminated HEA, coarse columnar grains are distributed throughout the sample while fine equiaxed grains indicated by the white arrows are formed near the melt pool boundaries, and the average grain size is found to be 24 ± 31 μm, which is much smaller than those of the two monolithic HEAs. This confirms the findings in Fig. 1(b). This means that the alternating printing may inhibit grain growth, leading to a measured grain size smaller than the predicted value based on the rule-of-mixture (ROM) principle.

The grain boundaries (GBs) are also affected by the alternating printing process. There are three distinct types of the GBs, i.e., the high-angle grain boundaries (HAGBs), the low-angle grain boundaries (LAGBs), and the sub-grain boundaries (SGBs). As the GBs map shows, the weighting of the different GBs in the laminated HEA does not correspond to the expected results based on the ROM. Most noticeably, the weighting of the SGBs in the laminated HEA far exceeds those in the two monolithic HEAs. Generally, SGBs are related to dislocations and are characterized by specific arrangements of dislocations. This implies that extra dislocations may be generated in

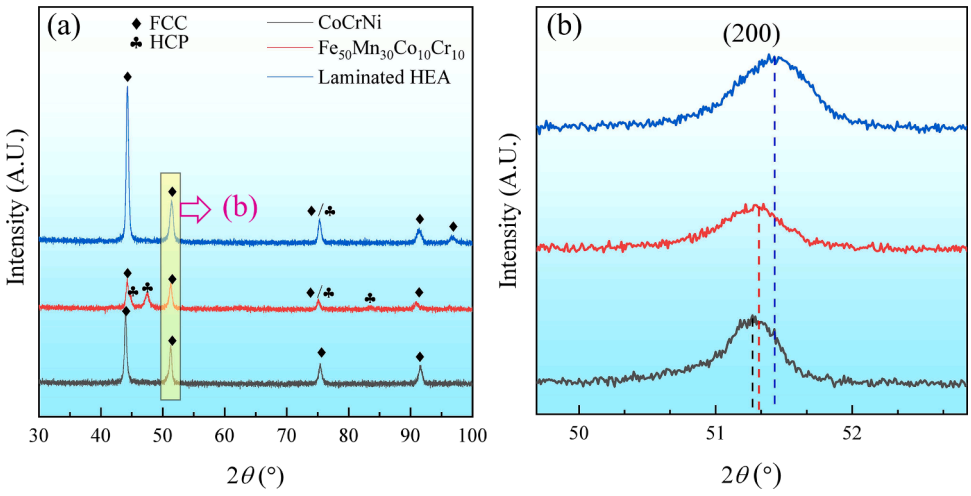

Fig. 1. (a) XRD patterns of the as-deposited laminated HEA, CoCrNi HEA, and $Fe_{50}Mn_{30}Co_{10}Cr_{10}$ HEA. (b) Enlarged view of the (200) diffraction peaks in (a).

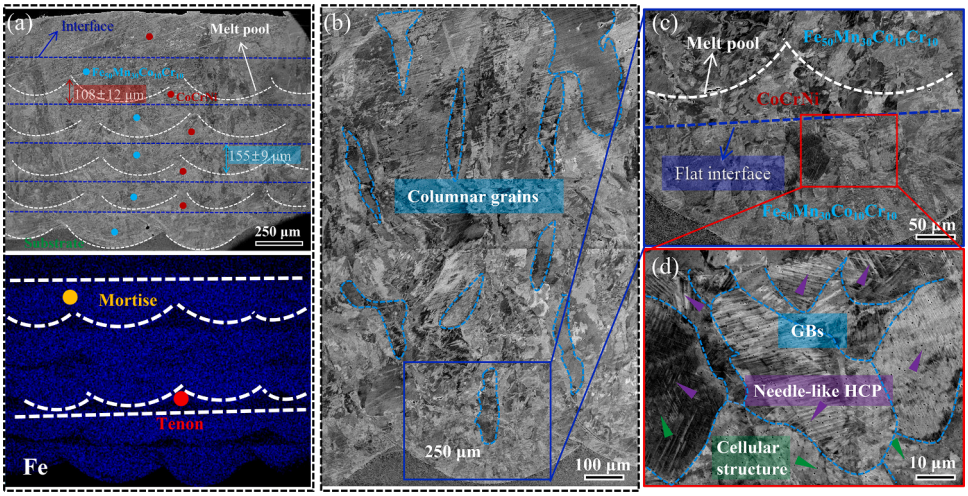

Fig. 2. (a) SEM image of the laminated HEA with Fe mappings. The focus is on the spatial distribution of Fe element to enhance the distinction between the CoCrNi layers and the $Fe_{50}Mn_{30}Co_{10}Cr_{10}$ layers. (b) ECCI images of the laminated HEA; (c) and (d) are the enlarged views of the two HEA components.

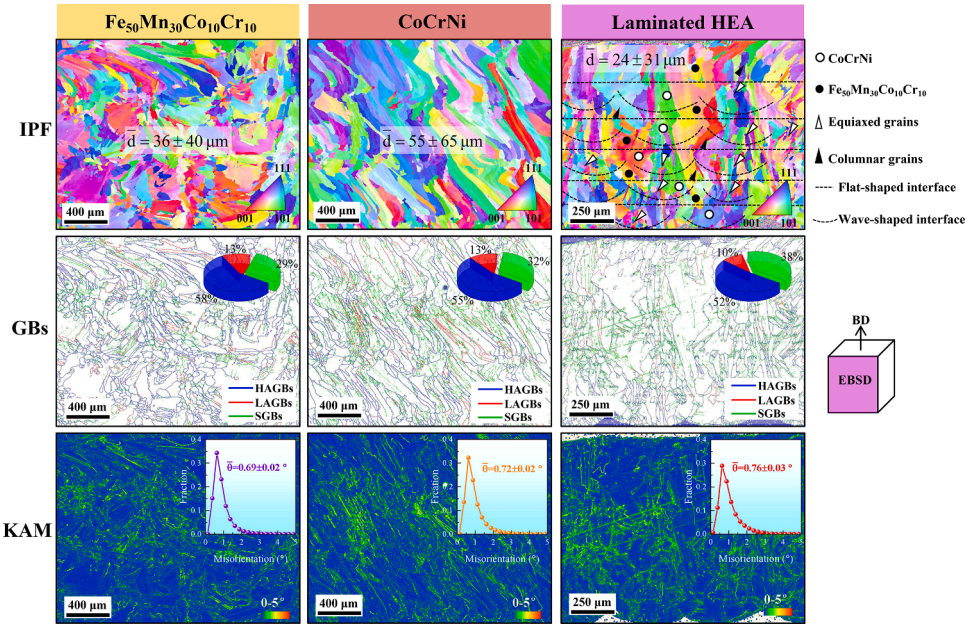

Fig. 3. EBSD results of the laminated HEA, pure CoCrNi, and $Fe_{50}Mn_{30}Co_{10}Cr_{10}$ HEAs including IPF maps, GBs maps, and KAM maps. Selected side view for EBSD scanning, where BD represents the building direction. The classification of the GBs is based on the following principle: HAGBs are those misorientations $> 15°$, LAGBs are those misorientations between 5 and 15°, and SGBs are those misorientations $< 5°$

the laminated HEA. This hypothesis is further supported by the kernel average misorientation (KAM) heat map. The KAM heat map reveals that the average KAM value of the laminated HEA is larger than those of the monolithic HEAs, indicating more severe plastic deformation in the laminated HEA.

The dislocation features of the laminated HEA are thoroughly characterized using TEM and HRTEM observations. Bright-field (BF) image in Fig. 4(a) reveals a visible interface. The EDS mappings shows from the upper left to the lower right, Fe and Mn is gradually increasing while Co, Cr and Ni is gradually decreasing. This proves that the transition from CoCrNi HEA to $Fe_{50}Mn_{30}Co_{10}Cr_{10}$ is achieved from the upper left to the lower right. A large number of dislocations are formed in the two HEA components. More specifically, in the CoCrNi region, the dislocations are observed in the form of dense dislocation lines and tangles, as shown in Fig. 4(b). Whereas, in the $Fe_{50}Mn_{30}Co_{10}Cr_{10}$ region, the dislocation structures have more complex geometry such as dislocation cells marked in Fig. 4(c), indicating that the dislocation evolution is more intense in the $Fe_{50}Mn_{30}Co_{10}Cr_{10}$ region.

The difference in the geometry of the dislocation structures may be attributed to the magnitude of the stacking fault energy (SFE) of the two HEAs. The SFE of the $Fe_{50}Mn_{30}Co_{10}Cr_{10}$ HEA is ~6.5 mJ/m^2 (Lu et al., 2018), which is lower than that of the CoCrNi HEA of ~22 mJ/m^2 (Laplanche et al., 2017). This indicates that dislocations in the former are more difficult to cross-slip, and in turn, the dislocation-dislocation interactions will be more active. Another possible key reason is the additional thermal history of the partial remelting event when the $Fe_{50}Mn_{30}Co_{10}Cr_{10}$ HEA is deposited, leading to spontaneous development of dislocations towards a low energy and self-stabilized structure (i.e., the dislocation cells). In addition to high dislocation density, a significant number of Lomer-Cottrell (L-C) locks are also formed in the laminated HEA. These L-C locks, observed in Fig. 4(d), are attributed to Shockley partial dislocation gliding on intersecting (111) and (11–1) planes. The atomic structure of the L-C lock is illustrated in the inset, revealing that the formation of the L-C locks is due to the intersection of respective dislocations on the (111) plane and (11–1) plane.

3.3. Local chemical variation (LCV) near the interfaces

Fig. 5(a) illustrates the elemental variation from the $Fe_{50}Mn_{30}Co_{10}Cr_{10}$ layer to CoCrNi layer and finally to $Fe_{50}Mn_{30}Co_{10}Cr_{10}$ layer. Clearly, the $Fe_{50}Mn_{30}Co_{10}Cr_{10}$ layer and CoCrNi layer still retain their initial chemical composition, and the diffusion effect of foreign elements is almost negligible. However, in the vicinity of the interfaces, the elements show inhomogeneous distribution, implying the interface boundary is not sharp but has a local chemical variation (LCV) zone. Specifically, near the flat-shaped interface marked by the green shadow, there is a marked chemical gradient. In the vicinity of the wavy-shaped interface marked by the purple shadow, the elements present a significant chemical fluctuation. The LCV zone of the wavy-shaped interface is much larger than that of the flat-shape interface zone, where the former is almost twice as larger as the latter.

Fig. 5(b) reveals the LCV in the vicinity of the flat-shaped interface. EDS mappings shows that when the $Fe_{50}Mn_{30}Co_{10}Cr_{10}$ layer to CoCrNi layer, the interface is easily identified. EDS lines depicts that the Fe and Mn elements rise suddenly while the Co, Cr and Ni elements drop suddenly when $Fe_{50}Mn_{30}Co_{10}Cr_{10}$ HEA crossing the interface. A marked chemical gradient exists within 5 μm away from the interface, followed by a gradual stabilization of the chemical variation and eventually in the formation of CoCrNi HEA. This indicates that although no remelting occurs near the flat-shaped interface, this interface is not completely sharp but has a compositional gradient within a very small interval (5 μm compared to the layer thickness of ~100 μm).

Fig. 5(c) reveals the LCV in the vicinity of the wavy-shaped interface. Compared to the flat-shaped interface, the wavy-shaped interface is not very visible. EDS mappings shows that there are no abrupt chemical changes on either side of the interface. This may be due to the partial remelting of the CoCrNi HEA, resulting in significant elemental diffusion and mixing. Intriguingly, with the help of Mn mapping, it can be found that dense chemical cells are formed in this zone. The chemical cells are caused by elemental

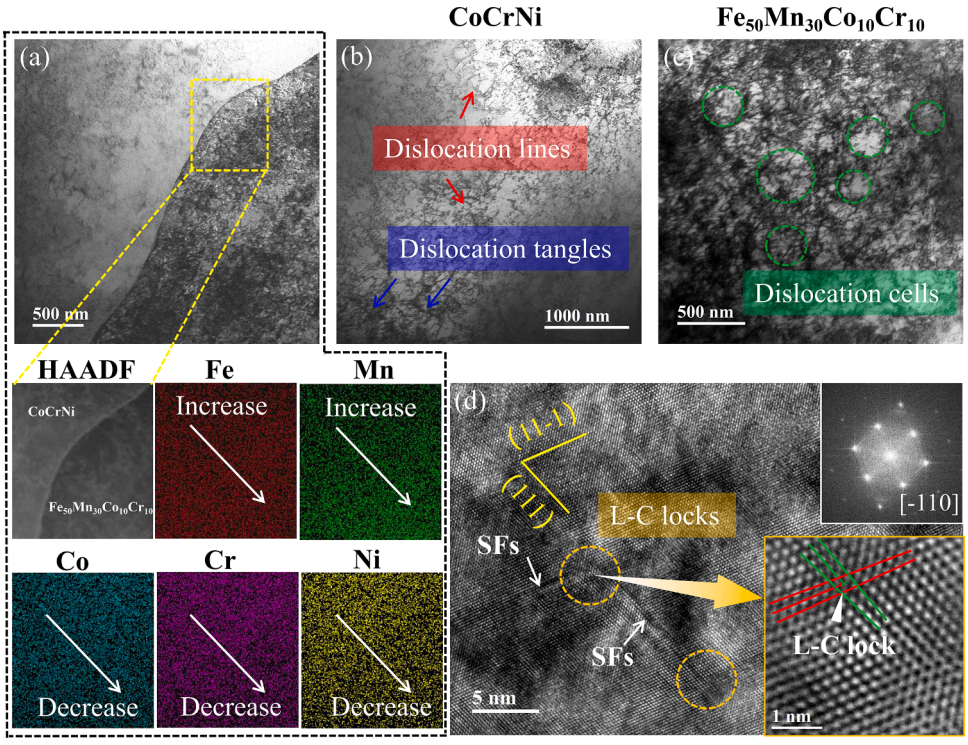

Fig. 4. TEM and HRTEM results of the laminated HEA. (a) BF images near the interface. EDS mappings showing a transition of CoCrNi HEA to $Fe_{50}Mn_{30}Co_{10}Cr_{10}$ from the upper left to the lower right. BF image of (b) CoCrNi layer and (c) $Fe_{50}Mn_{30}Co_{10}Cr_{10}$ layer. (d) HRTEM image of L-C locks within the laminated HEA. The inset is the atomic structure of an L-C lock marked in (d).

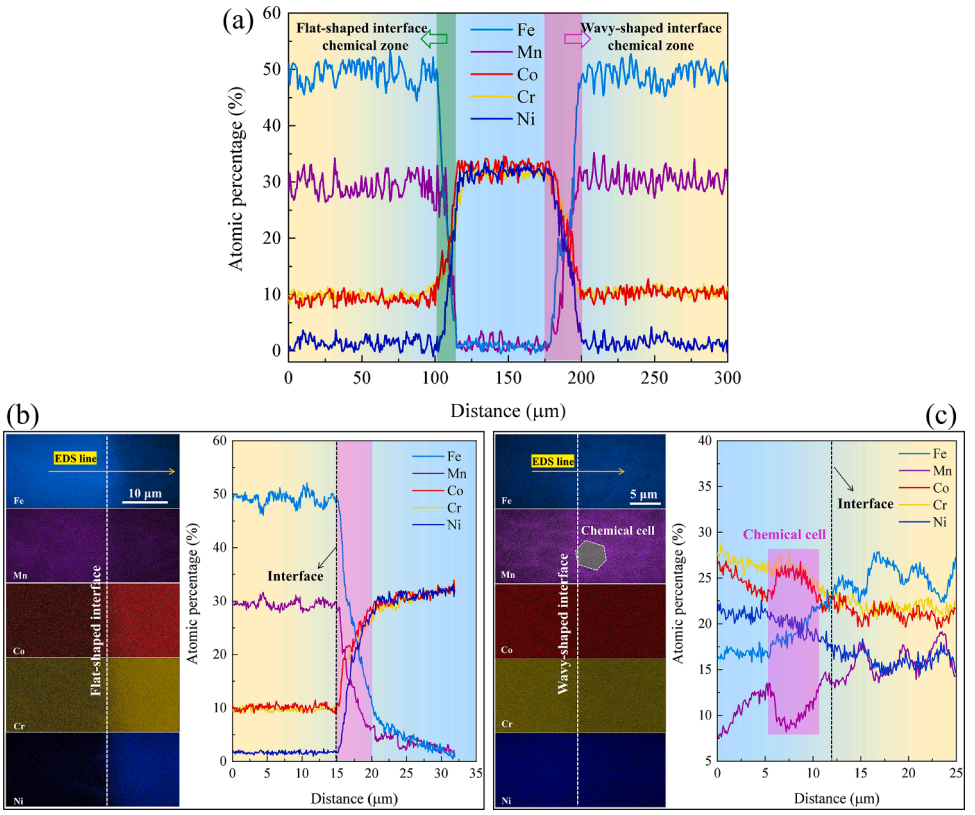

Fig. 5. (a) Local chemical variation from the $Fe_{50}Mn_{30}Co_{10}Cr_{10}$ layer to CoCrNi layer and finally to $Fe_{50}Mn_{30}Co_{10}Cr_{10}$ layer. (b) EDS mappings in the vicinity of the flat-shaped interface and the corresponding EDS lines from the $Fe_{50}Mn_{30}Co_{10}Cr_{10}$ layer to CoCrNi layer. (c) EDS mappings in the vicinity of the wavy-shaped interface and the corresponding EDS lines from the CoCrNi layer to $Fe_{50}Mn_{30}Co_{10}Cr_{10}$ layer.

segregation, most notably in the case of the Mn element (Thapliyal et al., 2021; Wang et al., 2020). Corresponding EDS lines demonstrates that in the vicinity of the wavy-shaped interface, there is a wide range (25 μm) of remarkable chemical fluctuation, confirming the existence of the chemical cells. (Note that although 25 μm may seem non-negligible, when 12.5 μm assigned to one side of the interface, compared to the layer thickness, it does not prevent the use of the ROM principle.)

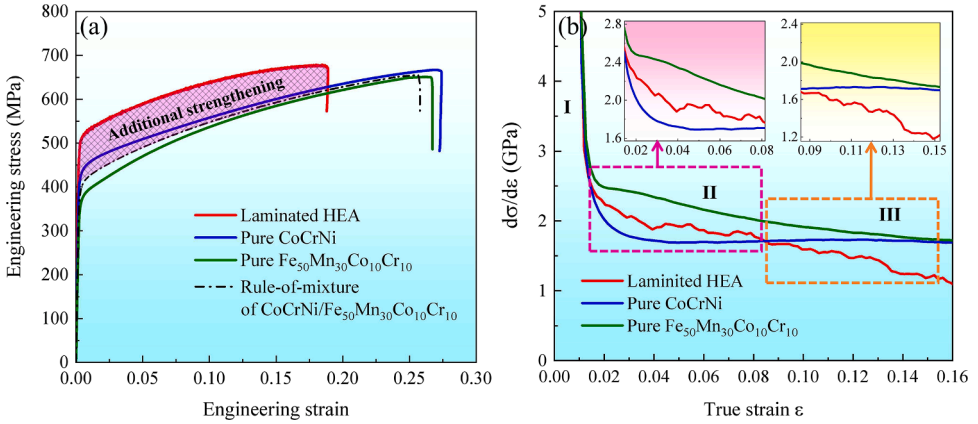

Fig. 6. (a) Typical engineering stress-strain curves of the various samples. The stress-strain curve of the laminated HEA indicates that there is extra strengthening compared with expectation from the rule-of-mixture. (b) The corresponding work hardening rates of various samples. The insets are the enlarged view at different strain stages marked in (b).

3.4. Mechanical properties

Fig. 6(a) displays the mechanical properties of all the samples. The values of the yield strength and uniform elongation are listed in Table 2. The yield strength and uniform elongation of the CoCrNi and $Fe_{50}Mn_{30}Co_{10}Cr_{10}$ HEAs are 405 ± 23 MP and 0.26 ± 0.01, 360 ± 25 MPa and 0.24 ± 0.02, respectively. According to the ROM, the yield strength and uniform elongation of the laminated HEA should be 378 MPa and 0.25, theoretically. Intriguingly, however, the measured values are 516 ± 13 MPa and 0.17 ± 0.01, respectively. The measured yield strength is 36.5 % higher than the theoretical value, indicating an additional strengthening existing in the laminated HEA, as shown by the shadow region. In terms of the uniform elongation, although the measured value is inferior to the theoretical value, the laminated HEA remains a reasonable uniform elongation.

Fig. 6(b) shows the work hardening rate of the various samples. Briefly, the work hardening rate can be divided into three stages. At stage I of the strain less than ~0.015, the work hardening rate of the laminated HEA is coincide with those of the two monolithic HEAs. At stage II of the strain between ~0.015 and ~0.09, the work hardening rate of the laminated HEA is in a state of compromise compared to those of the two monolithic HEAs. This indicates that within this strain interval, the laminated HEA inherits the excellent work hardening ability of the two HEAs. At stage III of the strain larger than ~0.09, the work hardening rate of the laminated HEA is lower than those of the two monolithic HEAs. Hardening ability of the laminated HEA loses due to, possibly, the weakening of interfaces between the two HEA layers in the late stage of the plastic deformation.

4. Discussion

4.1. Strengthening mechanisms

Compared to the expected value based on the ROM, the laminated HEA presents an improved yield strength due to extra strengthening. It is more encouraged that the extra strengthening results in yield strength that is superior to those of the CoCrNi and $Fe_{50}Mn_{30}Co_{10}Cr_{10}$ HEAs, rather than remaining in a compromised status. This is an inspiring event, and to our best knowledge, no similar events have been reported before. In general, for a laminated materials, the yield strength always follows a compromised principle (Chen et al., 2020; Guan et al., 2020; Huang et al., 2018; S. Liu et al., 2022; Ma et al., 2015; Tan et al., 2021; Wang et al., 2018, 2019), even if there is an extra strengthening beyond the predicted value using a ROM approach.

Extra strengthening in laminated structures is generally attributed to the interface strengthening. In addition, the specific value of the interface strengthening is usually obtained using the measured value minus the expected value (Wang et al., 2019). However, this is unfair because when two monolithic alloys are processed into a laminated alloy, the microstructures (e.g., grain size, texture, and dislocation density) that strongly affect the strength will change significantly. In this case, the ROM principle may be inappropriate. To clarify the concealed origin behind the enhanced yield strength of the laminated HEA and determine the exact value of the interface strengthening, a step-by-step analysis of the individual contributions of various strengthening is conducted.

4.1.1. Intrinsic strength

The laminated HEA is composited with the CoCrNi layers and the $Fe_{50}Mn_{30}Co_{10}Cr_{10}$ layers. Therefore, the intrinsic strength of the laminated HEA should obey a ROM principle, i.e., the intrinsic strength of the laminated HEA (σ_0) can be estimated as:

$$\sigma_0 = w_1\sigma_1 + w_2\sigma_2, \tag{1}$$

where σ_1 and σ_2 are the intrinsic strength of the CoCrNi HEA and the $Fe_{50}Mn_{30}Co_{10}Cr_{10}$ HEA, and w_1 and w_2 are the corresponding volume fraction. According to the respective layer thickness in Fig. 2(a), w_1 and w_2 are roughly estimated as 0.4 and 0.6, respectively. σ_1 and σ_2 are respectively calculated as 246.7 MPa and 157.8 MPa; see Supplementary materials. Therefore, the intrinsic strength (σ_0) of the laminated HEA is calculated as 194.2 MPa.

4.1.2. Grain boundary strengthening

Fig. 3(b) indicates that the laminated HEA contains three types of GBs, which should contribute to a large strength increment (Hansen, 2004). First, the HAGBs have the largest proportion of the total GBs and will make a remarkable contribution to the yield strength. In general, the contribution of the HAGBs to yield strength (σ_{HAGBs}) is the so-called Hall-Petch effect. A modified Hall-Petch formula is used to describe the HAGBs contribution (Luo et al., 2012), i.e.,

$$\sigma_{HAGBs} = k \cdot \left(\frac{L}{f}\right)^{-1/2}, \tag{2}$$

Table. 2
Yield stress and uniform elongation of various samples.

Samples	Yield stress (MPa)	Uniform elongation
CoCrNi	405 ± 23	0.26 ± 0.01
$Fe_{50}Mn_{30}Co_{10}Cr_{10}$	360 ± 25	0.24 ± 0.02
Laminated HEA	516 ± 13	0.17 ± 0.01
Based on ROM	378	0.25

where k is the Hall-Petch coefficient, L is the boundary spacing that can be deemed as the average equivalent grain size, and f is the fraction of the HAGBs.

Similar to the HAGBs, the LAGBs can also effectively impede dislocation movement and thus provide strengthening, which can be treated as the Taylor model. The equivalent dislocation density stored in LAGBs (ρ_{LAGBs}) is estimated by Hughes and Hansen (2000); Luo et al. (2012):

$$\rho_{LAGBs} = \frac{3(1-f)\theta_{LAGBs}}{bL}, \tag{3}$$

where b is the magnitude of the Burgers vector and θ_{LAGBs} is the average misorientation of the LAGBs. At least 10 LAGBs are counted to calculate the average misorientation; see Supplementary materials. The total dislocation density consists of two parts, i.e., the ρ_{LAGBs} and the original dislocation density. The strengthening contribution of the LAGBs (σ_{LAGBs}) can be expressed as (Luo et al., 2012):

$$\sigma_{LAGBs} = M\alpha Gb\sqrt{\rho_0 + \rho_{LAGBs}} - \sigma_\rho, \tag{4}$$

where M is the Taylor factor, α is a material constant, G is the shear modulus, and ρ_0 is the original dislocation density stored in the laminated HEA. σ_ρ represents the dislocation strengthening excluding the LAGBs strengthening effect, which will be analyzed in next. All the corresponding parameters are listed in Supplementary materials, and the σ_{HAGBs} and σ_{LAGBs} are calculated as ~65.8 MPa and ~1.3 MPa, respectively. Note that although the value of the σ_{LAGBs} is very small, it is still taken into account for coherence.

4.1.3. Dislocation strengthening

There are profuse SGBs in the laminated HEA. Generally, SGBs are inside independent grains and are often decorated with a high dislocation density (Bertsch et al., 2020). This has been verified by the TEM observations in Fig. 4, in which extensive dislocation tangles, dislocation cells, and L-C locks are observed. These complicated dislocation structures will significantly hinder dislocation slip, yielding a remarkable strengthening (Li et al., 2021; Xu et al., 2018). Therefore, the dislocation strengthening (σ_ρ) plays a crucial role in this laminated HEA, which can be expressed as (Y. Z. Li et al., 2022):

$$\sigma_\rho = M\alpha Gb\sqrt{\rho_0}, \tag{5}$$

ρ_0 in the laminated HEAs is roughly calculated by the Williamson-Hall (W-H) method, which is widely used to estimate the dislocation density in metals (He et al., 2016; Wang et al., 2023). In XRD data, the total peak broadening (β_T) is due to the two effects of crystallite size (β_D) and micro-strain (β_ε), i.e.,

$$\beta_T = \beta_D + \beta_\varepsilon, \tag{6}$$

from the Scherer equation, β_D can be expressed as:

$$\beta_D = \frac{K\lambda}{L\cos\theta}, \tag{7}$$

where K is a shape factor that is generally taken as 0.9, λ is the wavelength of Cu Ka radiation, and θ is the Bragg angle of the corresponding peak position. The peak broadening due to the microstrain, β_ε is given by:

$$\beta_\varepsilon = 4\varepsilon\tan\theta, \tag{8}$$

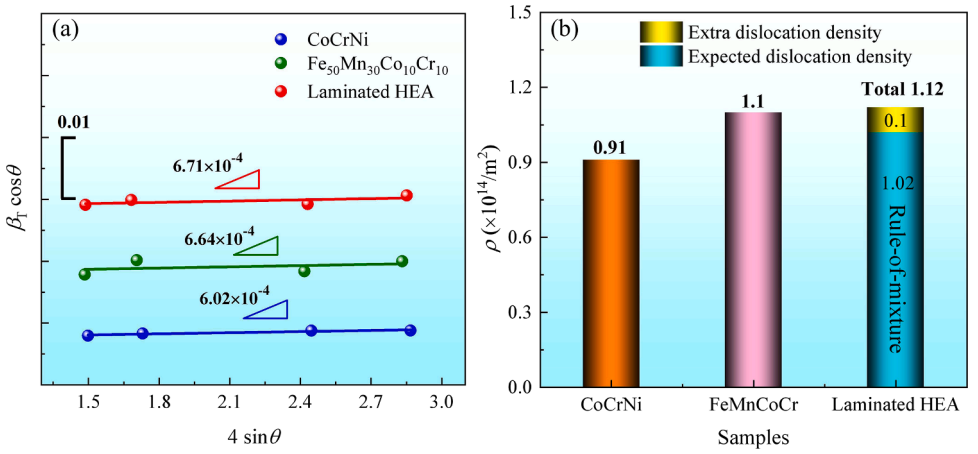

Fig. 7. (a) Plots of $b_T$cosq – 4sinq of various samples, where the slope of the linear fit showing the value of microstrain ε. (b) Corresponding dislocation density in the various samples.

where ε is the microstrain. Putting Eqs. (7) and (8) in Eqs. (6), Eq. (6) can be therefore rewritten as:

$$\beta_T \cos\theta = \frac{K\lambda}{L} + 4\varepsilon \sin\theta, \tag{9}$$

and the dislocation density is estimated as (Williamson and Smallman, 1956):

$$\rho_0 = 16.1\frac{\varepsilon^2}{b^2}. \tag{10}$$

Relations of $\beta_T\cos\theta - 4\sin\theta$ of all the samples are plotted in Fig. 7(a). From the W-H plot, the microstrain ε of the different samples (i.e., the slopes of the fitted lines) can be obtained, where the R^2 are 0.89, 0.35, 0.57 for the fitted data of the CoCrNi HEA, $Fe_{50}Mn_{30}Co_{10}Cr_{10}$ HEA and laminated HEA, respectively. The dislocation density is calculated and presented in Fig. 7(b). The total dislocation density in the laminated HEA is $1.12 \times 10^{14}\ m^{-2}$, which is higher than that in the two monolithic HEAs. Based on the ROM, the expected value of the dislocation density in the laminated HEA is $1.02 \times 10^{14}\ m^{-2}$, meaning that an extra dislocation density of $1 \times 10^{13}\ m^{-2}$ is generated, which is in good line with the findings in Fig. 3. According to Eq. (5), the σ_ρ of the CoCrNi HEA, the $Fe_{50}Mn_{30}Co_{10}Cr_{10}$ HEA, and the laminated HEA are calculated as 122.3, 128.6 and 134.9 MPa, respectively. Although the σ_ρ of the laminated HEA is large than the two monolithic HEAs, the increment is too small and insufficient to lead to a significant increase of yield strength.

4.1.4. *Interface strengthening*

The above strengthening mechanisms have been analyzed one by one, resulting in a total calculated value of 396.2 MPa. Although this is significant, it is lower than the measured yield strength of 516 MPa. Therefore, extra strengthening mechanisms must exist. In conventional laminated alloys, related studies have indicated that sharp or transition interfaces can provide graceful extra strengthening due to the GNDs hardening and back-stress strengthening (Huang et al., 2018; S. Liu et al., 2022; Ma et al., 2016, 2015; Wang et al., 2019). However, the strengthening indicated in the above studies are all for strain hardening during deformation, i.e., strengthening of the flow stress. In this work, the GNDs model and back-stress strengthening are inappropriate for the strengthening of the yield strength.

Fig.5 illustrates that although the laminated HEA maintains an alternating composite structure of the CoCrNi and $Fe_{50}Mn_{30}Co_{10}Cr_{10}$ HEAs, there are distinct LCV near the interfaces. Within these LCV zones, the distribution of elements is highly heterogeneous, which can strongly influence the mechanical properties (Ding et al., 2019). Previous experimental and theoretical investigations in various HEAs have demonstrated that LCV, such as ordering, clustering and fluctuation, can result in significant resistance to dislocation motion and consequently increased yield strength (Ding et al., 2019; Lei et al., 2018; J. Li et al., 2022, 2019; Pozuelo and Marian, 2024; Zhang et al., 2021). It is assumed that the extra strengthening is attributed to the interface strengthening through powerful dislocation-based mechanisms. Note that the interface strengthening here refers exclusively to dislocation-based strengthening (i.e., interface-dislocation interactions $\sigma_{I\text{-}D}$), excluding non-dislocation-based strengthening such as interface sliding. The value of the interface strengthening in this work is deduced as 119.8 MPa, accounting for ~23 % of the yield strength. All the strengthening mechanisms to strength contribution have been illustrated in Fig. 8. Clearly, if the interface strengthening is neglected, the yield strength of the laminated HEA has no advantage over the monolithic HEAs. The interface strengthening is the fundamental reason for the yield strength far exceeding the expected value. In addition, the interface strengthening is promising and even comparable to the dislocation strengthening.

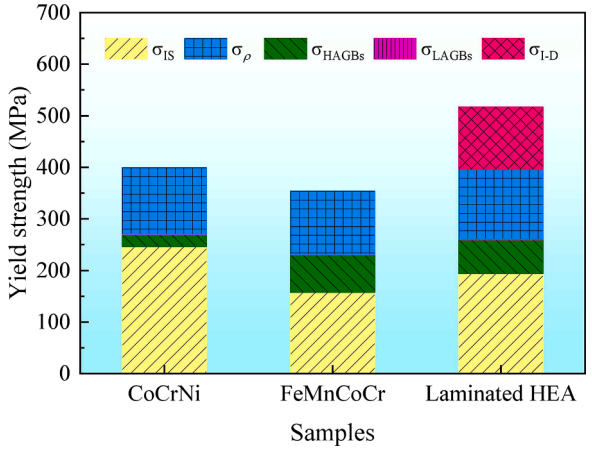

Fig. 8. Strength contribution of the various strengthening mechanisms. σ_{IS} represents the intrinsic strength.

4.2. LCV-dislocation interactions in the vicinity of interface

The interface strengthening is dislocation-based due to the LCV. A question naturally arises as to how the LCV interacts with dislocations to strengthen the laminated HEA. In this section, this question will be discussed in detail.

First, the LCV can tune the SFE distribution. Near the flat-shaped interface, the LCV can potentially result in a SFE gradient. Near the wavy-shaped interface, the LCV takes the form of chemical fluctuation, inevitably tuning the local SFE. SFE plays a crucial role in determining the mode of plastic deformation. The modulation of SFE caused by the LCV can potentially alter the local plastic deformation mechanisms, such as transitioning from planar slip to wavy slip (Lei et al., 2018), inducing double cross-slip (Bu et al., 2021), twinning (Zhang et al., 2021), and transformation. Consequently, the LCV can effectively impede dislocation motion, thereby enhancing the overall strength.

Second, the LCV can modify the distribution of the lattice friction and increase local internal stress (Ding et al., 2019). In the case of the flat-shaped interface, the local atomic strain field may change from tensile strain field to compressive strain filed (or vice versa) due to chemical gradient. In the case of the wavy-shaped interface with chemical fluctuation, the local atomic strain field would exhibit a pattern of alternating tensile-compressive strain fields. Consequently, both forms of LCV can lead to an inhomogeneous lattice strain, inducing unusual dislocation behaviors such as multiple kinks and jogs as well as double cross-slip (J. Li et al., 2022), and therefore strengthening.

In addition, LCV has the ability to tailor lattice distortion, thereby in turn trigging considerable solid-solution strengthening. The chemical fluctuation near the wavy-shaped interface is expected to greatly increase the lattice distortion due to the distinct mixing of elements in this region. As a result of the mixing of these five elements, the original ternary or quaternary composition becomes a quintuplet, leading to an increase in local atomic mismatch and consequently the lattice distortion. This heightened lattice distortion serves to intensify the dislocation pinning, thanks to the strong interactions between solute atoms and dislocations (Roy et al., 2021). Similarly, the chemical gradient near the flat-shaped interface also induces changes in the local lattice distortion. It can be envisioned that as one or more elements gradually increase, the lattice distortion and, consequently, the solute-dislocation interactions progressively intensify. Therefore, the LCV can provide a significant source of solid-solution strengthening.

Furthermore, it is important to consider the influence of other factors related to the LCV on dislocation motion. One is the presence of chemical cells within the LCV zone near the wavy-shaped interfaces. The chemical cells, often accompanied by dislocation cells, can

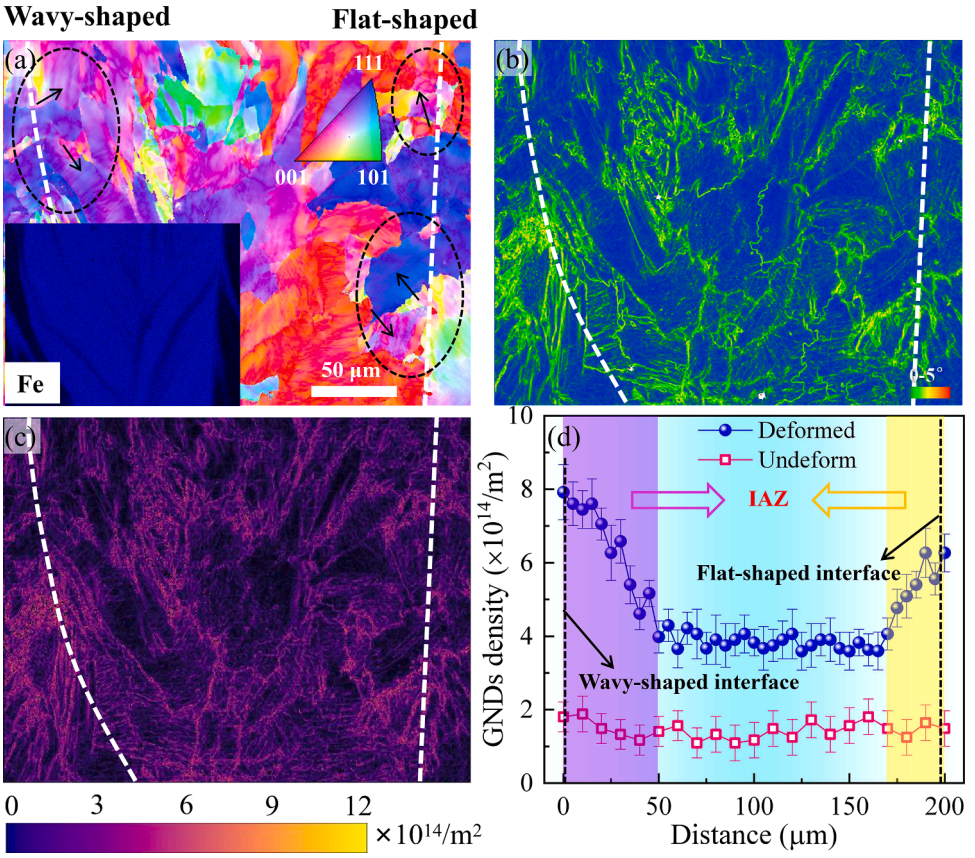

Fig. 9. (a) IPF map and (b) KAM heat map of the deformed laminated HEA strained to 0.07. (c) GNDs density map obtained based on the KAM data in (b). (d) Distribution of the GNDs density within the laminated HEA versus distance from the interfaces.

act as obstacles to dislocation motion (Li et al., 2022; Voisin et al., 2021; Wang et al., 2020). On the one hand, the chemical cell walls can effectively pin dislocations, impeding their motion. On the other hand, a high density of dislocations within the chemical cells have a higher likelihood of dissociation, resulting in the formation of wider stacking faults (SFs) that serve as barriers to dislocation motion (Voisin et al., 2021). Another potential important mechanism is the local chemical ordering, such as short-range order (SRO) strengthening. This phenomenon has been widely reported (Basu and De Hosson, 2020; Li et al., 2019; Yin et al., 2021; R. Zhang et al., 2020) in HEAs, and direct experimental observation of SRO has been conducted by Chen et al. (2021). The long-range LCV may promote the occurrence of the ordered structures and therefore strengthening. However, further detailed TEM characterization is required to confirm this hypothesis in the future.

4.3. Analysis of the variation in work hardening and the loss of ductility

In addition to the interface strengthening, it is also intriguing to note that the work hardening rate is divided into three distinct stages. Additionally, although the laminated HEA still retains reasonable plasticity, there is indeed a loss compared to the theoretical value. In this section, the origin of the variation in work hardening and the loss of ductility will be analyzed in detail.

4.3.1. Work hardening in stage I

At the stage I, the work hardening rate of the laminated HEA is almost coincides with that of the two monolithic HEAs, showing a sharp drop. This is a common or even intrinsic event at the early stage of plastic deformation, which is due to the early dislocation movement such as dislocation rearrangement and annihilation (Bai et al., 2022; Su et al., 2019; Wu et al., 2019).

4.3.2. Work hardening in stage II

At the stage II, the work hardening rate of the laminate HEA is in a state of compromise. This implies that the laminated HEA has an excellent strain hardening ability in this stage. In the laminated HEA, a significant mechanical incompatibility will be produced between the two HEA layers during deformation (Ma et al., 2016; Zhao et al., 2021). However, due to the strong bonding, the two HEA layers should be forced to deform together, thereby generating strain gradient in the vicinity of the interfaces to maintain co-deformation. Generally, the strain gradient is accommodated by the accumulation of GNDs (Gao et al., 1999; Gao and Huang, 2003; Li et al., 2020; Zhang et al., 2020; Zhao et al., 2021). Therefore, GNDs will be emitted from and gradually accumulated at the interfaces. Consequently, an extremely high density of GNDs should be formed and piled-up at the interfaces, resulting in considerable strain hardening.

Fig. 9(a) presents the IPF map of the deformed laminated HEA with a strain of 0.07. The Fe mapping is used to locate the interface. It is evident that there is a significant strain gradient near the two interfaces, as indicated by the color gradient marked by black arrows. Fig. 9(b) displays the KAM heat map, revealing that plastic deformation is more pronounced in the vicinity of the interfaces compared to the interior. This well supports that GNDs can accumulate effectively near the interfaces, leading to considerable strain hardening. In general, laminated alloys have an IAZ (Chen et al., 2020; Huang et al., 2018; Zhao et al., 2021). In this work, the IAZ of the flat-shaped interface and wavy-shaped interface is determined by the distribution of GNDs density versus the distance from interface. The GNDs density is calculated based on the KAM data in Fig. 9(b). Based on a strain gradient theory proposed by Gao et al. (1999), ρ_{GNDs} can be roughly calculated from KAM data (Calcagnotto et al., 2010), i.e.,

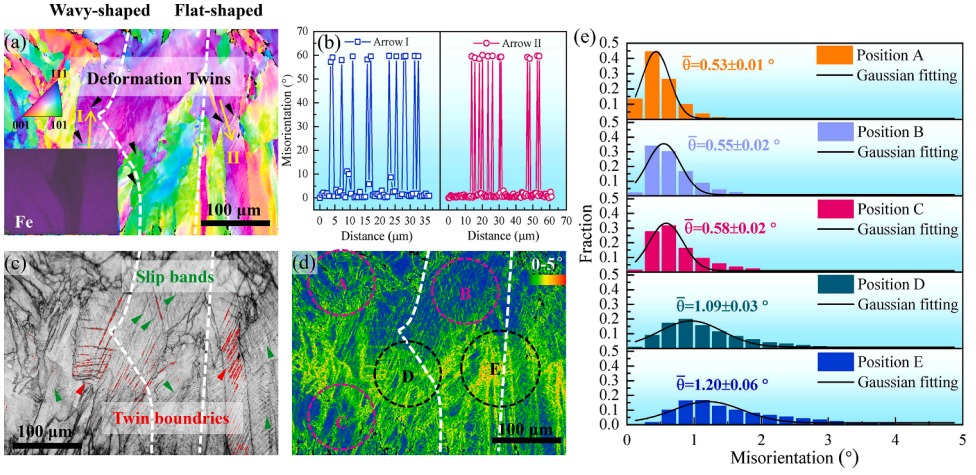

Fig. 10. EBSD results of the deformed laminated HEA strained to 0.12. (a) IPF map with Fe mapping. (b) Misorientation distribution of the two arrows marked in (a), confirming the presence of the deformation twins. (c) IQ map reflecting the severe band-like structures. (d) KAM heat map and (e) Corresponding KAM values of the positions near (D, E) and away from (A, B, C) the interfaces marked in (d).

$$\rho_{GNDs} = \frac{2\varphi}{\mu b}, \tag{11}$$

where φ is the local misorientation that can be obtained through KAM data, and μ is the EBSD scanning step size.

The GNDs density is shown in Fig. 9(c), indicating that the GNDs density is relatively high near the interfaces, particularly near the wavy-shaped interfaces. To analyze the distribution of GNDs density with respect to the distance from the interfaces, a method similar to (Ma et al., 2016) is employed. The GNDs density map is sliced parallel to the interface with a step of 5 μm, which is smaller than the grain size, to minimize the influence of non-interface effects such as grain boundaries and grain orientation. The average GNDs density within each slice is calculated and plotted against the corresponding distance from the interface in Fig. 9(d). Additionally, the distribution of GNDs density within the undeformed sample is provided as a baseline to eliminate inherent errors in EBSD measurement. It is evident that both the flat-shaped interface and wavy-shaped interface exhibit a distinct IAZ. The width of the IAZ of the wavy-shaped interface and flat-shaped interface is approximately 50 μm and 25 μm, respectively. This again confirms that the LCV can effectively strengthen the laminated HEA. Moreover, the maximum GNDs density near the wavy-shaped interface is higher than that near the flat-shaped interface, indicating that the wavy-shaped interface may be the primary source of strengthening.

4.3.3. Work hardening in stage III

At the stage III, the work hardening rate of the laminated HEA is inferior to that of the monolithic HEAs. To elucidate this phenomenon, the microstructures of the deformed laminated HEA with a strain of 0.12 are provided in Fig. 10. Fig. 10(a) shows that profuse deformation twins marked by black arrows are produced at/near the interfaces that are identified by the Fe mapping. Fig. 10 (b) is the misorientation distribution of the vectors across two twin colonies marked by yellow arrows in Fig. 10(a), confirming the presence of the deformation twins. Typically, deformation twins can occur under a relatively high strain condition since the critical resolved shear stress required for twinning is rather high. This means that the vicinity of the interfaces will undertake more severe plastic deformation than those locations away from the interfaces. This is verified by the image quality (IQ) map in Fig. 10(c). Clearly, the twin boundaries are mainly generated at/near the interfaces (in particular, the wavy-shaped interfaces). Whereas, at far distances from the interfaces, the local strain is small and insufficient to induce deformation twins but only slip bands marked by green arrows. Fig. 10(d) shows that the KAM at/near the interfaces (positions D and E) is significantly larger than that away from the interfaces (positions A, B, and C). The corresponding KAM values are provided in Fig. 10(e), indicating the value of the former is almost twice than the latter. All these results suggest that extensive heterogeneous interfaces can trigger severe plastic deformation and thus stress concentration in the late of stage of deformation, potentially weakening the interface and leading to premature cracking and fracture. This is probably the direct reason for stage III and why the uniform elongation of the laminated HEA is smaller than the expected value.

4.3.4. Analysis for the loss of ductility

As mentioned earlier, the deformation is more severe near the interfaces, which may induce severe stress concentration and possible cracking, ultimately resulting in premature fracture. Fig. 11(a) powerfully supports this hypothesis, as cracks are observed in

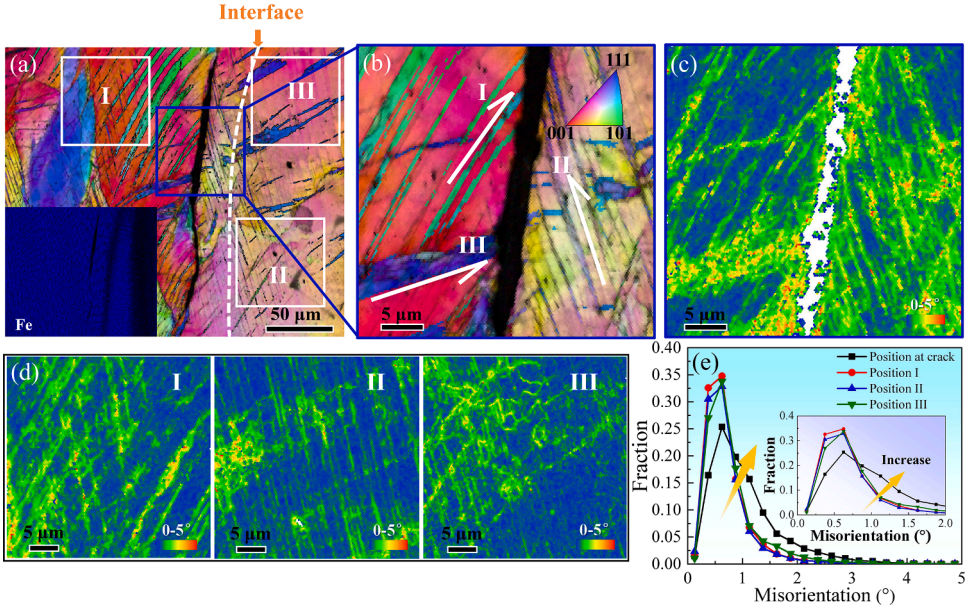

Fig. 11. Microstructures of the laminated HEA near the fracture surface. (a) IPF map with Fe mapping, showing the cracks formed in the $Fe_{50}Mn_{30}Co_{10}Cr_{10}$ region adjacent to interface. Enlarged view of the cracks in (a), showing multidirectional deformation twins. (c) KAM heat map of (b). (d) KAM heat maps of the positions I, II, III. (e) KAM distribution curves of (c) and (d), indicating larger plastic deformation at the cracks.

the $Fe_{50}Mn_{30}Co_{10}Cr_{10}$ region (determined by the Fe mapping) adjacent to the interfaces and develop along the interfaces. There are two main reasons for the cracks formed in this position. First, the stress concentration is more pronounced near the interfaces. Second, the $Fe_{50}Mn_{30}Co_{10}Cr_{10}$ HEA has a lower SFE compared to the CoCrNi HEA, which makes it more favorable for the generation of deformation twins and consequently severe plastic deformation. These two reasons would preferentially induce crack initiation in this region. Fig. 11(b) reveals a high density of deformation twins with multiple orientations (I, II, III) near of the cracks. These multi-directional twins intersect with each other, triggering intense twin-twin interactions that result in severe local plastic deformation. Fig. 11(c) and (d), the KAM heat maps, demonstrate that the cracks with multidirectional deformation twins exhibit more severe local plastic deformation compared to positions I, II, and III in Fig. 11(a) with unidirectional deformation twins. Fig. 11(e) shows that the peak of the KAM distribution at the cracks is significantly shifted to the right when compared to positions I, II, and III. This shift provides favorable evidence to validate the occurrence of severe local plastic deformation due to the intense twin-twin interactions. Therefore, it can be concluded that large plastic deformation near the interfaces leads to the formation of multidirectional deformation twins in the $Fe_{50}Mn_{30}Co_{10}Cr_{10}$ region. These multidirectional twins intersect with each other, resulting in intense twin-twin interactions. This, in turn, creates a large stress field that induces crack initiation and development along the interfaces, ultimately leading to premature fracture and the loss of ductility. However, despite the loss of ductility, the laminated HEA still maintains reasonable plasticity due to its excellent work hardening ability in the early deformation stage.

4.4. Advantages of wavy-shaped interface due to the M-T architecture

Compared with those laminated structures with only flat-shaped interfaces (Chen et al., 2020; Guan et al., 2020; S. Liu et al., 2022; Ma et al., 2016; Wang et al., 2019; Yang et al., 2022), the M-T architecture also contains extensive wavy-shaped interfaces besides the flat-shaped interfaces. Compared to the flat-shaped interface, the wavy-shaped interface has not only a larger LCV zone but also profuse chemical cells, which may lead to a more pronounced strain hardening during deformation.

A detailed TEM characterization near the two interfaces after deformation is provided. Fig. 12 illustrates the distinct differences in deformation features, including dislocations, SFs and deformation twins, between the two types of interfaces. In the case of dislocations, there is no visible distinction, as both exhibit a large number of dislocation aggregations, resulting in a high density of dislocation tangles. However, in terms of SFs and deformation twins, significant differences are observed. In the flat-shaped interface zone, only unidirectional SFs with a relatively low density are formed. Additionally, although deformation twins are present, they are sparsely distributed, with a thickness of 61.4 ± 21.9 nm. Whereas, the wavy-shaped interface zone exhibits a high density of SFs and deformation twins, which are densely distributed. Notably, in addition to the main SFs (I), numerous secondary SFs (II) are generated, forming dense intersections. These SF intersections induce strong SF-SF interactions, resulting in a significant resistance to dislocation movement and therefore strain strengthening. Furthermore, the thickness of the deformation twins within the wavy-shaped interface zone is 37.2 ± 12.1 nm, which is remarkable less than that within the flat-shaped interface. In general, a smaller thickness of twins corresponds to a more pronounced resistance to dislocation motion (Li et al., 2020), thus providing significant strain strengthening.

Fig. 13 is the morphology of the laminated HEA before and after deformation. Before deformation, the laminated HEA is filled with an intact M-T skeleton, and the interfaces between the two HEA layers are distinct. However, after deformation, while the overall M-T skeleton is retained, the M-T architecture is destroyed due to severe plastic deformation. In particular, near the wavy-shaped bulges marked by purple dashed circles, the interfaces here become blurred and are divided into several parts. Based on the findings presented in Figs. 12 and 13, it is confirmed that the wavy-shaped interface is more effective in impeding dislocation motion, establishing it as the primary source of strengthening.

5. Conclusion

In conclusion, a unique Mortise-Tenon (M-T) architecture of a laminated HEA, consisting of CoCrNi and $Fe_{50}Mn_{30}Co_{10}Cr_{10}$ HEAs, has been successfully fabricated using additive manufacturing. The strengthening and deformation mechanisms of this laminated HEAs are investigated in detail. Specifically, the crucial role played by the interfaces during deformation is systematically explained. This work fills a gap in this research field and provides a valuable reference for future research on laminated HEA. The main conclusions are summarized as follows.

(1) Due to the unique M-T architecture, the laminated HEA exhibits not only the typical flat-shaped interface but also a newly introduced wavy-shaped interface. This wavy-shaped interface is extensively observed and characterized in the laminated HEA.
(2) Typical local chemical variation (LCV) zones are present in the vicinity of both the flat-shaped and flat-shaped interfaces. The LCV can strongly interact with dislocations to produce extra interface strengthening. More intriguing, the LCV zone of the wavy-shaped interfaces is twice than that of the flat-shaped interface, and therefore the former has a larger interface-affected-zone. Consequently, the wavy-shaped interfaces play a critical role in promoting more significant interface strengthening.
(3) The unique M-T architecture not only enables extra strengthening, giving the laminated HEA superior strength compared to the two monolithic HEAs, but also shows the excellent work hardening ability in the early deformation, resulting in reasonable ductility.
(4) The designs of laminated HEAs and the resulting heterogeneous interface strengthening show great promise as strengthening strategies that can be compared to dislocation strengthening. This offers a new avenue for achieving strength-ductility synergistic enhancement in HEAs in the future.

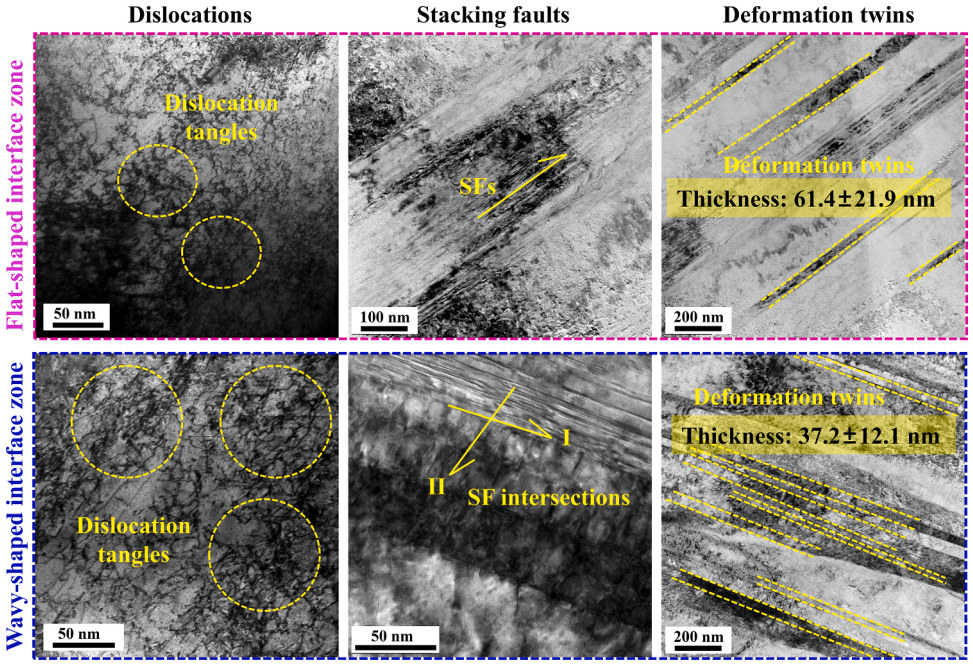

Fig. 12. Deformation features including dislocations, SFs, and deformation twins in the vicinity of the flat-shaped interface and wavy-shaped interface.

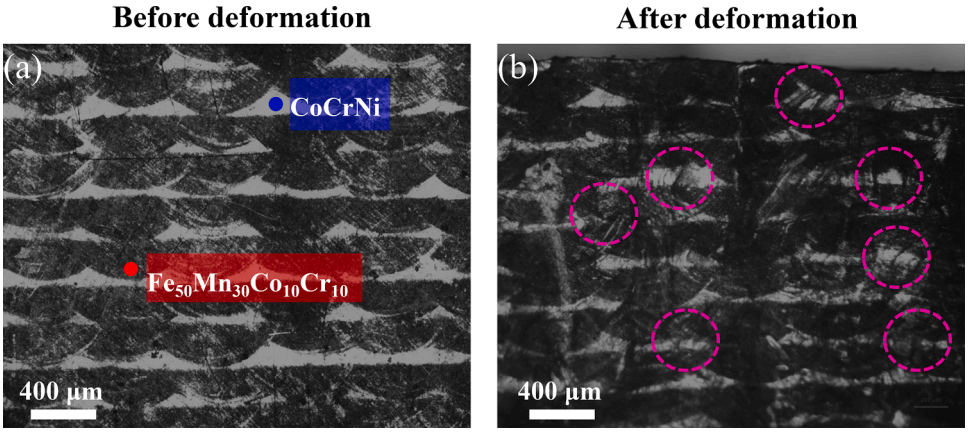

Fig. 13. Morphological changes of the M-T architecture (a) before and (b) after deformation.

CRediT authorship contribution statement

Yunjian Bai: Conceptualization, Methodology, Investigation, Writing – original draft, Writing – review & editing. **Yadong Li:** Conceptualization, Methodology, Investigation. **Yun-jiang Wang:** Conceptualization, Methodology, Formal analysis, Writing – review & editing. **Kun Zhang:** Conceptualization, Validation, Methodology, Resources, Writing – review & editing. **Quanyu Jiang:** Methodology, Investigation. **Zishang Liu:** Methodology, Investigation. **Zheng Hu:** Conceptualization. **Bingchen Wei:** Conceptualization, Validation, Supervision, Funding acquisition, Resources, Writing – review & editing.

Declaration of Competing Interest

The authors declare that they have no known competing financial interests or personal relationships that could have appeared to influence the work reported in this paper.

Data availability

Data will be made available on request.

Acknowledgments

This work was supported by the National Natural Science Foundation of China (Grant No. 12272392, No. 11790292), the Strategic Priority Research Program of the Chinese Academy of Sciences (Grant No. XDB22040303), and the Innovation Program (237099000000170004).

Supplementary materials

Supplementary material associated with this article can be found, in the online version, at doi:10.1016/j.ijplas.2023.103777.

References

Bai, Y., Jiang, H., Yan, K., Li, M., Wei, Y., Zhang, K., Wei, B., 2021. Phase transition and heterogeneous strengthening mechanism in CoCrFeNiMn high-entropy alloy fabricated by laser-engineered net shaping via annealing at intermediate-temperature. J. Mater. Sci. Technol. 92, 129–137. https://doi.org/10.1016/j.jmst.2021.03.028.

Bai, Y., Lyu, G.J., Wang, Y.J., Chen, T., Zhang, K., Wei, B., 2023. Laser shock peening strengthens additively manufactured high-entropy alloy through novel surface grain rotation. Mater. Sci. Eng. A 871, 144886. https://doi.org/10.1016/j.msea.2023.144886.

Bai, Y., Zhang, K., Chen, T., Liu, Z., Wang, Y., Wei, B., 2022. Alterable tension-compression asymmetry in work hardening of an additively manufactured dual-phase high-entropy alloy. Int. J. Plast. 158, 103432 https://doi.org/10.1016/j.ijplas.2022.103432.

Basu, I., De Hosson, J.T.M., 2020. Strengthening mechanisms in high entropy alloys: fundamental issues. Scr. Mater. 187, 148–156. https://doi.org/10.1016/j.scriptamat.2020.06.019.

Bertsch, K.M., Meric de Bellefon, G., Kuehl, B., Thoma, D.J., 2020. Origin of dislocation structures in an additively manufactured austenitic stainless steel 316L. Acta Mater. 199, 19–33. https://doi.org/10.1016/j.actamat.2020.07.063.

Bu, Y., Wu, Y., Lei, Z., Yuan, X., Wu, H., Feng, X., Liu, J., Ding, J., Lu, Y., Wang, H., Lu, Z., Yang, W., 2021. Local chemical fluctuation mediated ductility in body-centered-cubic high-entropy alloys. Mater. Today 46, 28–34. https://doi.org/10.1016/j.mattod.2021.02.022.

Cai, Y., Zhu, L., Cui, Y., Han, J., 2021. Manufacturing of FeCoCrNi + FeCoCrNiAl laminated high-entropy alloy by laser melting deposition (LMD). Mater. Lett. 289, 129445 https://doi.org/10.1016/j.matlet.2021.129445.

Calcagnotto, M., Ponge, D., Demir, E., Raabe, D., 2010. Orientation gradients and geometrically necessary dislocations in ultrafine grained dual-phase steels studied by 2D and 3D EBSD. Mater. Sci. Eng. A 527, 2738–2746. https://doi.org/10.1016/j.msea.2010.01.004.

Cantor, B., 2021. Multicomponent high-entropy Cantor alloys. Prog. Mater. Sci. 120, 100754 https://doi.org/10.1016/j.pmatsci.2020.100754.

Chen, W., He, W., Chen, Z., Jiang, B., Liu, Q., 2020. Extraordinary room temperature tensile ductility of laminated Ti/Al composite: roles of anisotropy and strain rate sensitivity. Int. J. Plast. 133, 102806 https://doi.org/10.1016/j.ijplas.2020.102806.

Chen, X., Wang, Q., Cheng, Z., Zhu, M., Zhou, H., Jiang, P., Zhou, L., Xue, Q., Yuan, F., Zhu, J., Wu, X., Ma, E., 2021. Direct observation of chemical short-range order in a medium-entropy alloy. Nature 592, 712–716. https://doi.org/10.1038/s41586-021-03428-z.

DebRoy, T., Wei, H.L., Zuback, J.S., Mukherjee, T., Elmer, J.W., Milewski, J.O., Beese, A.M., Wilson-Heid, A., De, A., Zhang, W., 2018. Additive manufacturing of metallic components – process, structure and properties. Prog. Mater. Sci. 92, 112–224. https://doi.org/10.1016/j.pmatsci.2017.10.001.

Ding, Q., Zhang, Y., Chen, X., Fu, X., Chen, D., Chen, S., Gu, L., Wei, F., Bei, H., Gao, Y., Wen, M., Li, J., Zhang, Z., Zhu, T., Ritchie, R.O., Yu, Q., 2019. Tuning element distribution, structure and properties by composition in high-entropy alloys. Nature 574, 223–227. https://doi.org/10.1038/s41586-019-1617-1.

Gao, H., Huang, Y., 2003. Geometrically necessary dislocation and size-dependent plasticity. Scr. Mater. 48, 113–118. https://doi.org/10.1016/S1359-6462(02)00329-9.

Gao, H., Huang, Y., Nix, W.D., Hutchinson, J.W., 1999. Mechanism-based strain gradient plasticity - I. Theory. J. Mech. Phys. Solids 47, 1239–1263. https://doi.org/10.1016/S0022-5096(98)00103-3.

Guan, S., Wan, D., Solberg, K., Berto, F., Welo, T., Yue, T.M., Chan, K.C., 2020. Additively manufactured CrMnFeCoNi/AlCoCrFeNiTi0.5 laminated high-entropy alloy with enhanced strength-plasticity synergy. Scr. Mater. 183, 133–138. https://doi.org/10.1016/j.scriptamat.2020.03.032.

Hansen, N., 2004. Hall-petch relation and boundary strengthening. Scr. Mater. 51, 801–806. https://doi.org/10.1016/j.scriptamat.2004.06.002.

Hasan, M.N., Liu, Y.F., An, X.H., Gu, J., Song, M., Cao, Y., Li, Y.S., Zhu, Y.T., Liao, X.Z., 2019a. Simultaneously enhancing strength and ductility of a high-entropy alloy via gradient hierarchical microstructures. Int. J. Plast. 123, 178–195. https://doi.org/10.1016/j.ijplas.2019.07.017.

Hasan, M.N., Liu, Y.F., An, X.H., Gu, J., Song, M., Cao, Y., Li, Y.S., Zhu, Y.T., Liao, X.Z., 2019b. Simultaneously enhancing strength and ductility of a high-entropy alloy via gradient hierarchical microstructures. Int. J. Plast. 123, 178–195. https://doi.org/10.1016/j.ijplas.2019.07.017.

He, J.Y., Wang, H., Huang, H.L., Xu, X.D., Chen, M.W., Wu, Y., Liu, X.J., Nieh, T.G., An, K., Lu, Z.P., 2016. A precipitation-hardened high-entropy alloy with outstanding tensile properties. Acta Mater. 102, 187–196. https://doi.org/10.1016/j.actamat.2015.08.076.

He, Z., Jia, N., Yan, H., Shen, Y., Zhu, M., Guan, X., Zhao, X., Jin, S., Sha, G., Zhu, Y., Liu, C.T., 2021. Multi-heterostructure and mechanical properties of N-doped FeMnCoCr high entropy alloy. Int. J. Plast. 139, 102965 https://doi.org/10.1016/j.ijplas.2021.102965.

Huang, C.X., Wang, Y.F., Ma, X.L., Yin, S., Höppel, H.W., Göken, M., Wu, X.L., Gao, H.J., Zhu, Y.T., 2018. Interface affected zone for optimal strength and ductility in heterogeneous laminate. Mater. Today 21, 713–719. https://doi.org/10.1016/j.mattod.2018.03.006.

Hughes, D.A., Hansen, N., 2000. Microstructure and strength of nickel at large strains. Acta Mater. 48, 2985–3004. https://doi.org/10.1016/S1359-6454(00)00082-3.

Laplanche, G., Kostka, A., Reinhart, C., Hunfeld, J., Eggeler, G., George, E.P., 2017. Reasons for the superior mechanical properties of medium-entropy CrCoNi compared to high-entropy CrMnFeCoNi. Acta Mater. 128, 292–303. https://doi.org/10.1016/j.actamat.2017.02.036.

Lei, Z., Liu, X., Wu, Y., Wang, H., Jiang, S., Wang, S., Hui, X., Wu, Y., Gault, B., Kontis, P., Raabe, D., Gu, L., Zhang, Q., Chen, H., Wang, H., Liu, J., An, K., Zeng, Q., Nieh, T.G., Lu, Z., 2018. Enhanced strength and ductility in a high-entropy alloy via ordered oxygen complexes. Nature 563, 546–550. https://doi.org/10.1038/s41586-018-0685-y.

Li, J., Chen, Y., He, Q., Xu, X., Wang, H., Jiang, C., Liu, B., Fang, Q., Liu, Y., Yang, Y., Liaw, P.K., Liu, C.T., 2022a. Heterogeneous lattice strain strengthening in severely distorted crystalline solids. Proc. Natl. Acad. Sci. U. S. A. 119, 1–7. https://doi.org/10.1073/pnas.2200607119.

Li, Q.J., Sheng, H., Ma, E., 2019. Strengthening in multi-principal element alloys with local-chemical-order roughened dislocation pathways. Nat. Commun. 10, 1–11. https://doi.org/10.1038/s41467-019-11464-7.

Li, S.H., Zhao, Y., Radhakrishnan, J., Ramamurty, U., 2022b. A micropillar compression investigation into the plastic flow properties of additively manufactured alloys. Acta Mater. 240, 118290 https://doi.org/10.1016/j.actamat.2022.118290.
Li, X., Lu, L., Li, J., Zhang, X., Gao, H., 2020. Mechanical properties and deformation mechanisms of gradient nanostructured metals and alloys. Nat. Rev. Mater. 5, 706–723. https://doi.org/10.1038/s41578-020-0212-2.
Li, Y.Z., Liang, Z.Y., Huang, M.X., 2022c. Strengthening contributions of dislocations and twins in warm-rolled TWIP steels. Int. J. Plast. 150 https://doi.org/10.1016/j.ijplas.2021.103198.
Li, Z., Cui, Y., Yan, W., Zhang, D., Fang, Y., Chen, Y., Yu, Q., Wang, G., Ouyang, H., Fan, C., Guo, Q., Xiong, D.B., Jin, S., Sha, G., Ghoniem, N., Zhang, Z., Wang, Y.M., 2021. Enhanced strengthening and hardening via self-stabilized dislocation network in additively manufactured metals. Mater. Today 50, 79–88. https://doi.org/10.1016/j.mattod.2021.06.002.
Li, Z., Pradeep, K.G., Deng, Y., Raabe, D., Tasan, C.C., 2016. Metastable high-entropy dual-phase alloys overcome the strength-ductility trade-off. Nature 534. https://doi.org/10.1038/nature17981.
Li, Z., Tasan, C.C., Pradeep, K.G., Raabe, D., 2017. A TRIP-assisted dual-phase high-entropy alloy: grain size and phase fraction effects on deformation behavior. Acta Mater. 131, 323–335. https://doi.org/10.1016/j.actamat.2017.03.069.
Liu, D., Yu, Q., Kabra, S., Jiang, M., Forna-kreutzer, P., Zhang, R., Payne, M., Walsh, F., Gludovatz, B., Asta, M., Minor, A.M., George, E.P., Ritchie, R.O., 2022. Exceptional fracture toughness of CrCoNi-based medium- and high-entropy alloys at 20 kelvin 983, 978–983.
Liu, L., Zhang, Y., Li, J., Fan, M., Wang, X., Wu, G., Yang, Z., Luan, J., Jiao, Z., Liu, C.T., Liaw, P.K., Zhang, Z., 2022b. Enhanced strength-ductility synergy via novel bifunctional nano-precipitates in a high-entropy alloy. Int. J. Plast. 153, 103235 https://doi.org/10.1016/j.ijplas.2022.103235.
Liu, S., Xia, D., Yang, H., Huang, G., Yang, F., Chen, X., Tang, A., Jiang, B., Pan, F., 2022c. Mechanical properties and deformation mechanism in Mg-Gd alloy laminate with dual-heterostructure grain size and texture. Int. J. Plast. 157, 103371 https://doi.org/10.1016/j.ijplas.2022.103371.
Lu, W., Liebscher, C.H., Dehm, G., Raabe, D., Li, Z., 2018. Bidirectional transformation enables hierarchical nanolaminate dual-phase high-entropy alloys. Adv. Mater. 30, 1–10. https://doi.org/10.1002/adma.201804727.
Luo, P., McDonald, D.T., Xu, W., Palanisamy, S., Dargusch, M.S., Xia, K., 2012. A modified Hall-Petch relationship in ultrafine-grained titanium recycled from chips by equal channel angular pressing. Scr. Mater. 66, 785–788. https://doi.org/10.1016/j.scriptamat.2012.02.008.
Ma, X., Huang, C., Moering, J., Ruppert, M., Höppel, H.W., Göken, M., Narayan, J., Zhu, Y., 2016. Mechanical properties of copper/bronze laminates: role of interfaces. Acta Mater. 116, 43–52. https://doi.org/10.1016/j.actamat.2016.06.023.
Ma, X.L., Huang, C.X., Xu, W.Z., Zhou, H., Wu, X.L., Zhu, Y.T., 2015. Strain hardening and ductility in a coarse-grain/nanostructure laminate material. Scr. Mater. 103, 57–60. https://doi.org/10.1016/j.scriptamat.2015.03.006.
Miracle, D.B., Senkov, O.N., 2017. A critical review of high entropy alloys and related concepts. Acta Mater. 122, 448–511. https://doi.org/10.1016/j.actamat.2016.08.081.
Niu, P., Li, R., Fan, Z., Yuan, T., Zhang, Z., 2021. Additive manufacturing of TRIP-assisted dual-phases Fe50Mn30Co10Cr10 high-entropy alloy: microstructure evolution, mechanical properties and deformation mechanisms. Mater. Sci. Eng. A 814, 141264. https://doi.org/10.1016/j.msea.2021.141264.
Pan, Q., Zhang, L., Feng, R., Lu, Q., An, K., Chuang, A.C., Poplawsky, J.D., Liaw, P.K., Lu, L., 2021. Gradient cell–structured high-entropy alloy with exceptional strength and ductility. Science 374, 984–989. https://doi.org/10.1126/science.abj8114 (80-.).
Pozuelo, M., Marian, J., 2024. In-situ observation of 'chemical' strengthening induced by compositional fluctuations in Nb-Mo-Ta-W. Scr. Mater. 238, 115750 https://doi.org/10.1016/j.scriptamat.2023.115750.
Qin, S., Yang, M., Jiang, P., Wang, J., Wu, X., Zhou, H., Yuan, F., 2022. Designing structures with combined gradients of grain size and precipitation in high entropy alloys for simultaneous improvement of strength and ductility. Acta Mater. 230, 117847 https://doi.org/10.1016/j.actamat.2022.117847.
Ren, J., Zhang, Y., Zhao, D., Chen, Y., Guan, S., Liu, Y., Liu, L., Peng, S., Kong, F., Poplawsky, J.D., Gao, G., Voisin, T., An, K., Wang, Y.M., Xie, K.Y., Zhu, T., Chen, W., 2022. Strong yet ductile nanolamellar high-entropy alloys by additive manufacturing 608. 10.1038/s41586-022-04914-8.
Roy, A., Sreeramagiri, P., Babuska, T., Krick, B., Ray, P.K., Balasubramanian, G., 2021. Lattice distortion as an estimator of solid solution strengthening in high-entropy alloys. Mater. Charact. 172, 110877 https://doi.org/10.1016/j.matchar.2021.110877.
Sathiyamoorthi, P., Kim, H.S., 2022. High-entropy alloys with heterogeneous microstructure: processing and mechanical properties. Prog. Mater. Sci. 123, 100709 https://doi.org/10.1016/j.pmatsci.2020.100709.
Su, J., Raabe, D., Li, Z., 2019. Hierarchical microstructure design to tune the mechanical behavior of an interstitial TRIP-TWIP high-entropy alloy. Acta Mater. 163, 40–54. https://doi.org/10.1016/j.actamat.2018.10.017.
Tan, C., Chew, Y., Duan, R., Weng, F., Sui, S., Ng, F.L., Du, Z., Bi, G., 2021. Additive manufacturing of multi-scale heterostructured high-strength steels. Mater. Res. Lett. 9, 291–299. https://doi.org/10.1080/21663831.2021.1904299.
Tang, Y., Li, D.Y., 2022. Dynamic response of high-entropy alloys to ballistic impact. Sci. Adv. 8, 1–9. https://doi.org/10.1126/sciadv.abp9096.
Thapliyal, S., Agrawal, P., Agrawal, P., Nene, S.S., Mishra, R.S., McWilliams, B.A., Cho, K.C., 2021. Segregation engineering of grain boundaries of a metastable Fe-Mn-Co-Cr-Si high entropy alloy with laser-powder bed fusion additive manufacturing. Acta Mater. 219, 117271 https://doi.org/10.1016/j.actamat.2021.117271.
Voisin, T., Forien, J.B., Perron, A., Aubry, S., Bertin, N., Samanta, A., Baker, A., Wang, Y.M., 2021. New insights on cellular structures strengthening mechanisms and thermal stability of an austenitic stainless steel fabricated by laser powder-bed-fusion. Acta Mater. 203 https://doi.org/10.1016/j.actamat.2020.11.018.
Wang, H., Zhu, Z.G., Chen, H., Wang, A.G., Liu, J.Q., Liu, H.W., Zheng, R.K., Nai, S.M.L., Primig, S., Babu, S.S., Ringer, S.P., Liao, X.Z., 2020. Effect of cyclic rapid thermal loadings on the microstructural evolution of a CrMnFeCoNi high-entropy alloy manufactured by selective laser melting. Acta Mater. 196, 609–625. https://doi.org/10.1016/j.actamat.2020.07.006.
Wang, Q., Dong, Y., Jiang, Z., Huang, J., 2023. Enhancing low thermal expansion behavior and strength via induced Zr-rich intermetallic phase in Fe-36Ni Invar alloy. Mater. Des. 226, 111644 https://doi.org/10.1016/j.matdes.2023.111644.
Wang, Y., Yang, M., Ma, X., Wang, M., Yin, K., Huang, A., Huang, C., 2018. Improved back stress and synergetic strain hardening in coarse-grain/nanostructure laminates. Mater. Sci. Eng. A 727, 113–118. https://doi.org/10.1016/j.msea.2018.04.107.
Wang, Y.F., Wang, M.S., Fang, X.T., Guo, F.J., Liu, H.Q., Scattergood, R.O., Huang, C.X., Zhu, Y.T., 2019. Extra strengthening in a coarse/ultrafine grained laminate: role of gradient interfaces. Int. J. Plast. 123, 196–207. https://doi.org/10.1016/j.ijplas.2019.07.019.
Weng, F., Chew, Y., Zhu, Z., Yao, X., Wang, L., Ng, F.L., Liu, S., Bi, G., 2020. Excellent combination of strength and ductility of CoCrNi medium entropy alloy fabricated by laser aided additive manufacturing. Addit. Manuf. 34, 101202 https://doi.org/10.1016/j.addma.2020.101202.
Williamson, G.K., Smallman, R.E., 1956. III. Dislocation densities in some annealed and cold-worked metals from measurements on the X-ray Debye-Scherrer spectrum. Philos. Mag. 1, 34–46. https://doi.org/10.1080/14786435608238074.
Wu, H., Huang, M., Li, X., Xia, Y., Wang, Z., Fan, G., 2021. Temperature-dependent reversed fracture behavior of multilayered TiBw/Ti-Ti(Al) composites. Int. J. Plast. 141, 102998 https://doi.org/10.1016/j.ijplas.2021.102998.
Wu, Q., He, F., Li, J., Kim, H.S., Wang, Z., Wang, J., 2022. Phase-selective recrystallization makes eutectic high-entropy alloys ultra-ductile. Nat. Commun. 13 https://doi.org/10.1038/s41467-022-32444-4.
Wu, S.W., Wang, G., Jia, Y.D., Yi, J., Zhai, Q.J., Liu, C.T., Sun, B.A., Chu, H.J., Shen, J., Liaw, P.K., Zhang, T.Y., 2019. Enhancement of strength-ductility trade-off in a high-entropy alloy through a heterogeneous structure. Acta Mater. 165, 444–458. https://doi.org/10.1016/j.actamat.2018.12.012.
Wu, X., Yang, M., Yuan, F., Wu, G., Wei, Y., Huang, X., Zhu, Y., 2015. Heterogeneous lamella structure unites ultrafine-grain strength with coarse-grain ductility. Proc. Natl. Acad. Sci. U. S. A. 112, 14501–14505. https://doi.org/10.1073/pnas.1517193112.
Xu, X.D., Liu, P., Tang, Z., Hirata, A., Song, S.X., Nieh, T.G., Liaw, P.K., Liu, C.T., Chen, M.W., 2018. Transmission electron microscopy characterization of dislocation structure in a face-centered cubic high-entropy alloy Al0.1CoCrFeNi. Acta Mater. 144, 107–115. https://doi.org/10.1016/j.actamat.2017.10.050.
Yang, T., Zhao, Y.L., Tong, Y., Jiao, Z.B., Wei, J., Cai, J.X., Han, X.D., Chen, D., Hu, A., Kai, J.J., Lu, K., Liu, Y., Liu, C.T., 2018. Multicomponent intermetallic nanoparticles and superb mechanical behaviors of complex alloys. Science 362, 933–937. https://doi.org/10.1126/science.aas8815 (80-.).
Yang, Y., Chen, T., Tan, L., Poplawsky, J.D., An, K., Wang, Y., Samolyuk, G.D., Littrell, K., Lupini, A.R., Borisevich, A., George, E.P., 2021. Bifunctional nanoprecipitates strengthen and ductilize a medium-entropy alloy. Nature 595, 245–249. https://doi.org/10.1038/s41586-021-03607-y.

Yang, Y., Hu, J., Liu, X.Y., Xu, W., Li, B., Ling, G.P., Pang, X.Y., Tian, Y.Z., 2022. Post treatment of an additively manufactured composite consisting of 304L stainless steel and CoCrFeMnNi high-entropy alloy. Mater. Sci. Eng. A 831. https://doi.org/10.1016/j.msea.2021.142104.

Yeh, J.W., Chen, S.K., Lin, S.J., Gan, J.Y., Chin, T.S., Shun, T.T., Tsau, C.H., Chang, S.Y., 2004. Nanostructured high-entropy alloys with multiple principal elements: novel alloy design concepts and outcomes. Adv. Eng. Mater. 6, 299–303. https://doi.org/10.1002/adem.200300567. +274.

Yin, S., Zuo, Y., Abu-Odeh, A., Zheng, H., Li, X.G., Ding, J., Ong, S.P., Asta, M., Ritchie, R.O., 2021. Atomistic simulations of dislocation mobility in refractory high-entropy alloys and the effect of chemical short-range order. Nat. Commun. 12, 1–14. https://doi.org/10.1038/s41467-021-25134-0.

Zhang, J.Y., He, Q.F., Li, J., Yang, Y., 2021. Chemical fluctuation enabling strength-plasticity synergy in metastable single-phase high entropy alloy film with gigapascal yield strength. Int. J. Plast. 139 https://doi.org/10.1016/j.ijplas.2021.102951.

Zhang, R., Zhao, S., Ding, J., Chong, Y., Jia, T., Ophus, C., Asta, M., Ritchie, R.O., Minor, A.M., 2020a. Short-range order and its impact on the CrCoNi medium-entropy alloy. Nature 581, 283–287. https://doi.org/10.1038/s41586-020-2275-z.

Zhang, X., Gui, Y., Lai, M., Lu, X., Gu, J., Wang, F., Yang, T., Wang, Z., Song, M., 2023. Enhanced strength-ductility synergy of medium-entropy alloys via multiple level gradient structures. Int. J. Plast. 164, 103592 https://doi.org/10.1016/j.ijplas.2023.103592.

Zhang, Y., Cheng, Z., Lu, L., Zhu, T., 2020b. Strain gradient plasticity in gradient structured metals. J. Mech. Phys. Solids 140. https://doi.org/10.1016/j.jmps.2020.103946.

Zhao, J., Zaiser, M., Lu, X., Zhang, B., Huang, C., Kang, G., Zhang, X., 2021. Size-dependent plasticity of hetero-structured laminates: a constitutive model considering deformation heterogeneities. Int. J. Plast. 145, 103063 https://doi.org/10.1016/j.ijplas.2021.103063.

Zhu, Y., Wu, X., 2023. Heterostructured materials. Prog. Mater. Sci. 131, 101019 https://doi.org/10.1016/j.pmatsci.2022.101019.